Efficient Confinement of Solid Capacity Booster Powder as Monolithic Structures for High Performance Redox Mediated Flow Batteries

Gimena Marin-Tajadura, Yi He, Virginia Ruiz, and Edgar Ventosa**

Confinement of solid electroactive materials in the external reservoirs of Redox-Mediated Flow Batteries (RMFB) is of critical importance for the development of this family of battery technologies. Herein, an efficient strategy that is based on a flow-through configuration is proposed. Confinement of all solid particles in a single porous block (so-called monolith) that occupies the entire reservoir brings practical and fundamental advantages. The improved flow distribution across the reservoir for the flow-through configuration enables enhanced kinetics and utilization rates (twice the utilization rate in 20% shorter time). Pressure drop induced by the flow-through configuration is easily reduced by changing the reservoir geometry becoming negligible in comparison to the drop induced by the cell (value for the monolith can be as low as 0.2% of the cell value). Additionally, determination of intrinsic properties of the steady monolith prior to its encapsulation enables knowing textural properties of the reservoir which are required for fundamental aspects. While ferrocyanide – Prussian Blue (redox mediator – solid booster) is used as model system here, the versatility of this strategy enables its implementation in other systems including future chemistries.

1. Introduction

Renewable energy sources such as solar or wind power will be crucial for the transition from fossil-fuels to a more sustainable energy production. However, its unpredictable and intermittent nature requires efficient and cost-effective energy storage systems to match energy production and demand.[1] Among energy storage systems, redox flow batteries (RFB) are especially suitable for large-scale stationary applications, offering competitive advantages over conventional batteries such as cost-effectiveness and long cycle life.[2] Moreover, energy storing materials in RFB are dissolved in electrolyte solutions stored in external reservoirs, which determine energy, while power is associated with the electrochemical reactor. This provides RFB with the intrinsic capability for independent scalability of power and energy, which offers great system flexibility. Despite the advantages of RFB, a major challenge of existing flow battery technologies is their low energy density, which is limited by the solubility of the electroactive species in the electrolyte. A strategy to increase energy density in RFB is storing charge in solid electroactive materials, which can be implemented in two ways: 1) as slurries flowing through the entire system in the case of semisolid flow batteries; 2) being confined in the external reservoirs and electrically connected to the electrochemical reactor by charge carriers (redox mediators) dissolved in the flowing electrolytes in the case of redox-mediated flow batteries (RMFB).[3] Confining the solid active material (or solid booster) in the external reservoirs, outside the energy conversion reactor, allows energy and power to remain decoupled in RMFB. In this configuration energy storage reservoirs become chemical reactors where the confined solid energy storing material and flowing redox mediators undergo heterogeneous charge transfer reactions. Reacted redox mediators act as molecular wires carrying charges between the energy storage reservoirs (chemical reactors) and the energy conversion (electrochemical) reactor. Hence, development of RMFB technology requires optimization of materials and processes occurring at both reactor types as well as careful reactor design considerations. Since RMFB employ the conventional configuration of RFB, improvements related to design of the electrochemical cell power stacks in RMFB will be driven by progress achieved in RFB.[4] On the other hand, key engineering aspects for further improvement and practical deployment of RMFB are related to the external reservoirs (chemical reactors), as stated by well-established researchers in RMFB technology in recent perspective articles.[3,5] An optimized design of the chemical reactor is crucial to promote kinetic and transport processes in order

---

G. Marin-Tajadura, Y. He, V. Ruiz, E. Ventosa
International Research Center in Critical Raw Materials-ICCRAM
University of Burgos
Pza. Misael Bañuelos s/n, Burgos E-09001, Spain
E-mail: vrfernandez@ubu.es; eventosa@ubu.es

G. Marin-Tajadura, Y. He, V. Ruiz, E. Ventosa
Department of Chemistry
University of Burgos
Pza. Misael Bañuelos s/n, Burgos E-09001, Spain

The ORCID identification number(s) for the author(s) of this article can be found under https://doi.org/10.1002/aenm.202404501

DOI: 10.1002/aenm.202404501

to achieve optimal energy and power density with high material utilization, robust cycling performance, and minimum maintenance, especially upon scaling up the system.

Despite the consensus on the critical importance of reactor design engineering, this aspect is scarcely addressed in RMFB research. Thus, most research efforts in RMFB have focused on materials rather than engineering solutions, with a broad range of new redox mediators and solid active materials having been researched.[5a,6] Conversely, fewer studies are devoted to studies of chemical reactor design by exploring how solid booster packing and experimental conditions such as reactor height, redox mediator concentration, solution flow rate or operating temperature affect the molar conversion of the solid electroactive material in a packed bed flow reactor.[7] Such studies conclude that conversion in the case of a fast redox process is limited by diffusion of redox mediators in the solution phase through the booster aggregates, highlighting how critical efficient packing of solid electroactive materials in the reservoirs is. Booster particles should be densely packed to maximize energy density, while keeping facile and homogeneous flow of redox electrolyte solution. In RMFB reports, solid materials are usually loaded in the tank in the form of dispersed particles[8] or powder,[9] as films/coatings,[10] pellets[11] or granules[12] of different sizes and shapes to achieve dense packing. Different approaches have been proposed to tune the microstructure (porosity, pore size distribution and tortuosity) of booster pellets, mostly consisting on the addition of sacrificial fillers, binders and surfactants in the preparation of dense pellets that are later removed by solvent leaching or thermal treatment to produce porous pellets.[11] However, regardless of the booster format (granules or pellets), internal porosity and packing density, microchannels are formed between pellets or granules (inter-pellet porosity), hindering the desired flow through the core of pellets (or granules) and leading to a so-called flow-by configuration. Such a "flow-by" regime prevents efficient utilization of the solid booster material. Even in the case of packed bed flow reactors where the electrolyte is forced to "flow through" the booster bed, the loosely packed powder/particles are not totally immobilized and hence preferential flow channels will be formed.

In this work, we present an advantageous strategy for efficiently packing and immobilizing booster materials as a single monolithic structure in the external reservoirs of RMFB. The manufacturing methodology is straightforward, easily scalable and versatile in terms of material chemistries and booster composition (carbon additive can be added to tune porosity as there is no need to sinter). We illustrate how the monolith configuration offers several advantages originating from the fixed position of the solid material in the tank. On the one hand, a filtering effect of the electrolyte "flowing-through" the whole booster material is ensured, minimizing dead volume and preventing formation of preferential flow pathways. This allows efficient redox mediator diffusion to the electroactive sites and faster reaction kinetics to attain higher booster utilization rates, which is advantageous from a practical point of view. Moreover, as the monolith occupies the full tank volume, the tank porosity can be easily determined as it corresponds to the monolith internal porosity. This allows accurate validation of the fundamental equation proposed to estimate the projected theoretical capacity attainable when scaling-up the tank, making the monolith configuration also useful from a more fundamental viewpoint. Furthermore, we will show that a priori expected pressure drop induced by flow resistance through the monolith can be easily tuned by the monolith dimensions becoming almost negligible considering the pressure drop induced by the electrochemical cell. Experimental results are fully supported by computer modeling, which predicts the advantages of booster confinement in a monolithic structure.

2. Results and Discussion

2.1. Modeling of Flow Distribution for Flow-By Versus Flow-Through Configurations

Achieving a homogenous flow distribution of the electrolyte throughout the entire volume of the reservoir is of key importance to ensure efficient utilization of solid booster material. In the most widely used confinement strategy, pellets are confined in the external reservoir. In such a case, pore size distribution will have at least two contributions: the porosity inside the pellets and the porosity between pellets. Since the pore size between pellets is significantly larger than that inside the densely packed pellets, the flow will preferentially go through the microchannels formed between pellets. This situation is referred to as flow-by since the flow cannot be forced to go through the core of multiple pellets. Molecular wiring for many active sites in the core of the pellets will depend on chemical diffusion of the redox mediators. One way to force the flow to go through the pellet is to prepare a single "giant pellet" that completely occupies all the space in the reservoir. In this case, the porosity between pellets would be eliminated, and the porosity of the reservoir would be equal to the intrinsic porosity of the "giant pellet". To differentiate the two structures, the giant pellet is refereed to as monolith since it is a large immobile structure. Numerical simulations were carried out to illustrate the theoretical flow distributions for the two scenarios (details in Section S1; Figures S1 and S2, Supporting Information). A more homogenous flow distribution is obtained for the case of "flow-through" in the single monolith, compared to the "flow-by" in the conventional random pellet architecture (**Figure 1**), which will facilitate access to more solid active sites. It should be noted that the same flow rate of 30 mL min^{-1} used in the simulations was maintained at the pump speed used for both types of booster confinements, that is, pellet and monolith.

2.2. Preparation and Encapsulation of Monoliths

To test the predicted advantages of a monolithic configuration of the solid booster, a new manufacturing method of the booster package was developed. With the aim of tuning material loading and porosity for an optimal electrolyte flow and material utilization, the manufacturing method was improved using the widely used and low-cost iron (III) hexacyanoferrate (II) (Prussian Blue) as model solid active material (commercially available). A number of parameters were varied to yield the best preparation protocol of Prussian Blue (PB) monoliths, which essentially consists of two main steps. First, slurries comprising PB, Ketjen Black (KB) and polyvinylidene fluoride (PVDF) in N-methyl-2-pyrrolidone

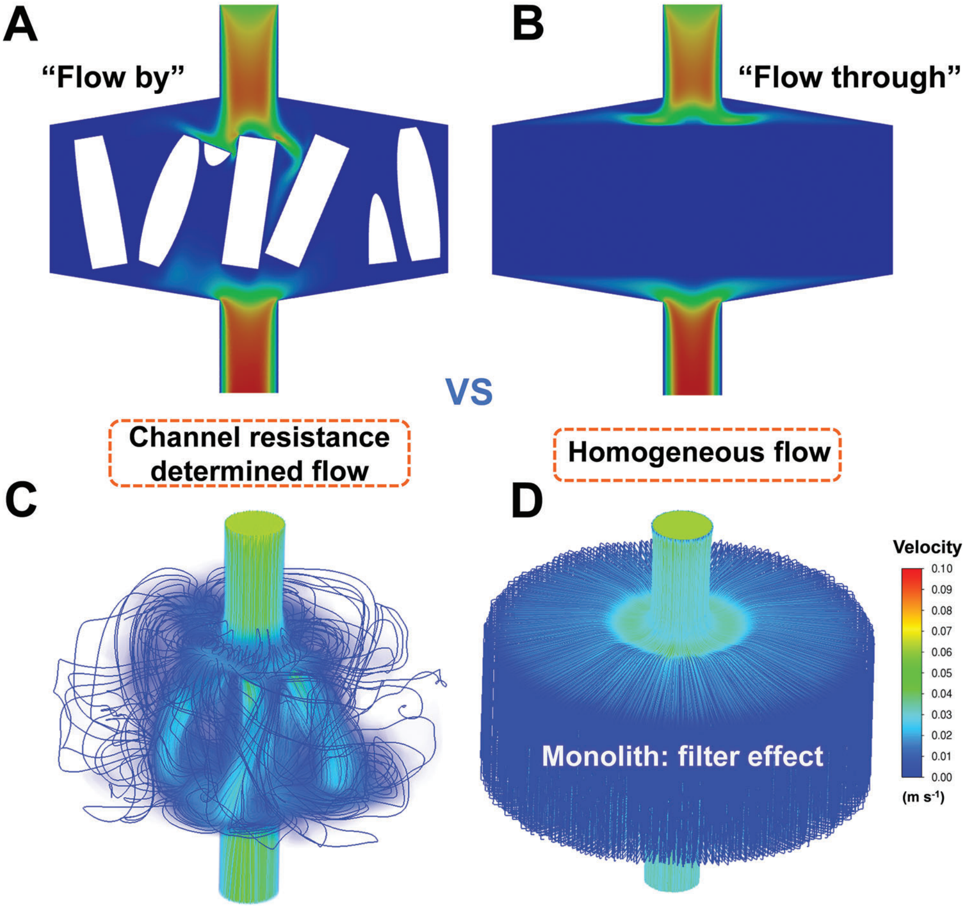

Figure 1. A,B) Velocity field and C,D) velocity tracking lines comparison of the fluid flow across A,B) the conventional pellet and C,D) the proof-of-the-concept monolith structure tank through FVM simulation.

(NMP) were blended using a high-shear mixer (Ultra Turrax IKA T25). Second, slurries were poured into cylindrical Teflon moulds and subsequently dried in an oven at 100 °C for 48 h. Once dried, cylindrical monoliths of smaller volumes than the mould were obtained. Applying this procedure, a number of monoliths with different compositions and sizes were prepared, as well as replicates to assess the reproducibility of the method (Section S2; Table S3, Supporting Information). Specifically, three slurry compositions with different PB content were tested, having 75:15:10, 80:10:10, and 85:05:10 in weight% (PB:KB:PVDF). Lower binder contents (<10%) were also used but resulted in less stable monoliths without modification of the drying conditions. Varying the relative ratio of the three slurry components required adjusting the solvent volume, for example KB-rich compositions demand more NMP to produce the slurry. In addition, the scalability of the method was also interrogated by preparing monoliths of four different sizes (0.8–14 mL), which involved scaling up slurry preparation and drying in larger moulds. Monoliths were characterized by measuring their dimensions (height and diameter) with a digital Vernier caliper and determining their porosity according to the C20-00 ASTM standard test method (Section S2; Figure S10; Table S3, Supporting Information). It is worth noting that very similar porosities were noted (70 ± 2%) in a large number of monoliths prepared (≈30), highlighting the reproducibility of the manufacturing method. Moreover, the similar porosity as well as other performance features, such as utilization rate, that will be discussed in following sections (Section 2.5) highlights the reproducibility and scalability of the monolith fabrication procedure in the investigated size range.

Finally, monoliths were encapsulated in reservoirs printed by stereolithography with an Anycubic Photon Mono 2 printer (Section S3; Figure S11, Supporting Information), using UV-sensitive 405 nm resin (Anycubic). The reservoir consisted of three pieces (**Figure 2A**), designed with Tinkercad and tailored to encapsulate each monolith size (Figure S12, Supporting Information). The monolith was inserted in the cylindrical piece with a bottom mesh and sealed to its walls with silicone to ensure electrolyte flow through the monolith. This piece was joined to the other two ones having inlet and outlet tubes using UV-sensitive 405 nm resin in a UV curing station. Once the monolith was encapsulated, it was connected with tubes to the electrochemical cell and electrolyte reservoir at the outlet of the electrochemical reactor (Figure 2B; Figure S13, Supporting Information).

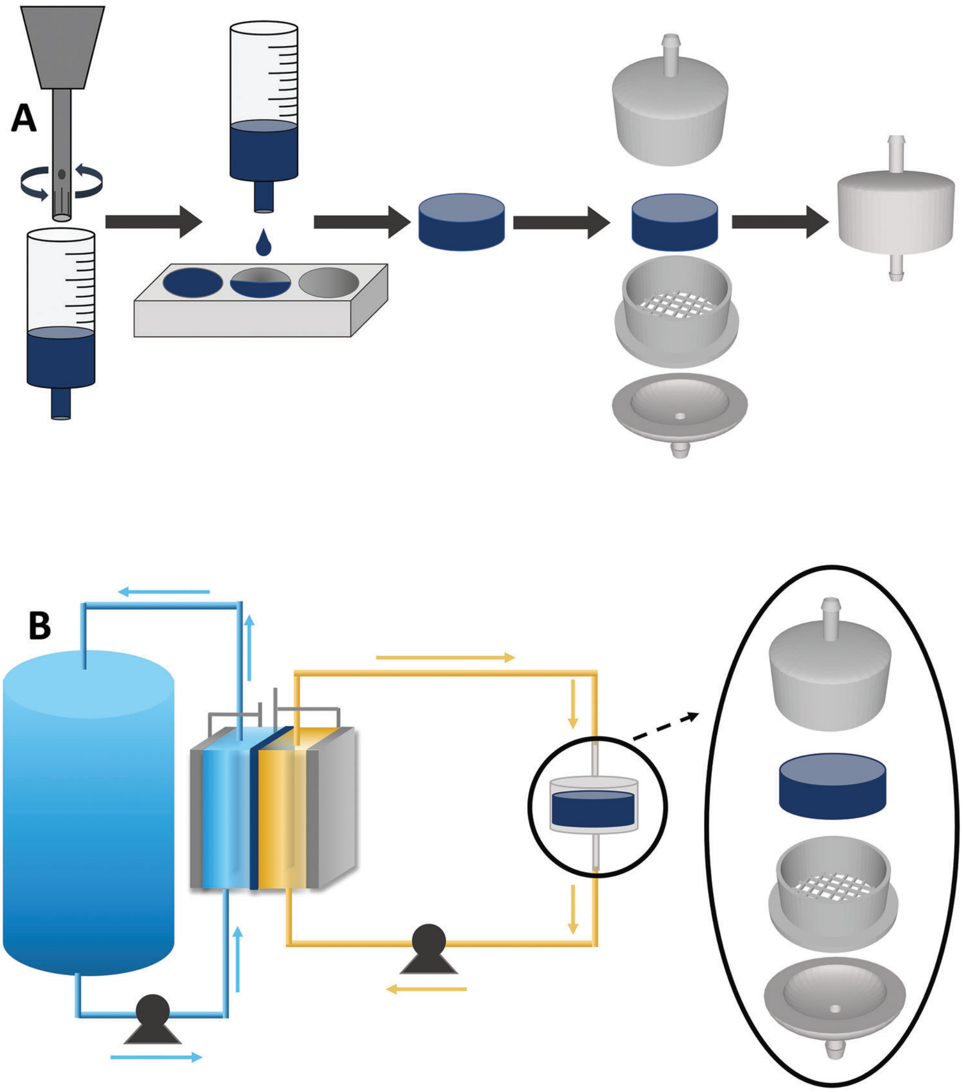

Figure 2. A) Schematics of the monolith preparation procedure. B) Schematics of the experimental set-up illustrating the location of the booster tank in the flow cell.

2.3. Electrochemical Performance of a Monolithic Booster

The redox-mediated reaction between electrolyte species and solid active material in the monolith (PB) was explored in a symmetric ferro-/ferricyanide redox flow cell having an oversized compartment as the non-capacity limiting side (NCLS) and the booster material in the other compartment, the capacity limiting side (CLS). For comparative purposes, the same loading of booster material was tested both in the form of pellets and monolith under identical conditions. Specifically, a symmetric ferro-/ferricyanide redox flow cell having 50 mL of a 0.2 м $K_4Fe(CN)_6$ and 0.1 м $K_3Fe(CN)_6$ mixture in the NCLS and 14 mL of 0.1 м of $K_3Fe(CN)_6$ in the CLS was used. The booster package, containing either pellets or a monolith, was inserted in a separate tank (the 3-piece encapsulating reservoir in Figure 2) in the CLS, connected to the electrochemical cell and electrolyte reservoir at the outlet of the electrochemical reactor. The booster tank was loaded with either pellets (1.329 g) or a monolith (1.323 g), both prepared from slurries with identical composition (80 PB:10 KB:10 PVDF) and hence, roughly the same amount of PB. The kinetics of the electrochemical reaction between the potassium ferro-/ferricyanide redox mediator and PB in pellets or monolith was investigated by applying a constant voltage (CV) of ±0.3 V with 10 mA cm^{-2} cut-off current density. Current density profiles for oxidation and reduction with both types of booster packages show higher current densities reached for monolith than pellets (Figure S14, Supporting Information). Thus, a charge capacity of 78.9 mAh was achieved with the monolith compared to 59.6 mAh with pellets. However, in order to overcome possible current density limitations due to the expanded graphite current collector, the same comparative power test was conducted this time including copper endplates on both sides of the electrochemical cell to improve electrical contact. The same weights of monolith (1.271 g) and pellets (1.289 g) with identical composition (80 PB:10 KB:10 PVDF) were again used to ensure testing similar amounts of PB. In this case, higher capacities were reached for

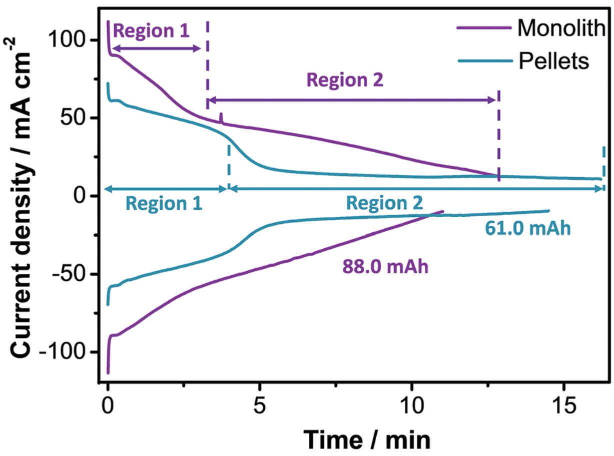

Figure 3. Current profile during oxidation and reduction at ±0.3 V (with 10 mA cm^{-2} cut-off current density) of a symmetric redox flow cell comprising 50 mL of a 0.2 M $K_4Fe(CN)_6$ and 0.1 M $K_3Fe(CN)_6$ mixture in the NCLS and 14 mL of 0.1 M $K_3Fe(CN)_6$ in the CLS, where boosters were added as either pellets or a monolith. Copper endplates were used to improve electrical contact with current collector.

both booster confinement formats, with the monolith again outperforming pellets in terms of higher current densities achieved, leading to increased oxidation and reduction capacities in shorter times (**Figure** 3). Specifically, the monolith and pellet configurations delivered a capacity of 51 mAh (50 mAh g^{-1}, 62.5% utilization rate) in 13 min and 24 mAh (23 mAh g^{-1}, 28.8% utilization rate) in 16 min, respectively, for 0.1 M of redox mediator. Note that the values are obtained after subtracting the contribution of the theoretical value of the electrolyte. Importantly, the apparent low utilization rate for pellets is attributed to the demanding cycling conditions of the experiments. Under the demanding conditions that are required for practical uses, kinetics becomes more relevant. Interestingly, two distinct plateaus were observed in the oxidation/reduction current profile of the symmetric flow cell with the monolith solid booster. The two plateaus are attributed to redox processes occurring at PB active sites inside the monolith with different accessibility for the electrolyte flow. Such assumption is supported by pore size distribution results from mercury porosimetry, which revealed two different pore size populations in all tested monoliths; one of 10–200 nm diameter nanopores and a second one of 5–25 µm diameter micropores (Section S5; Figure S15, Supporting Information). Thus, first plateau (Region 1) would correspond to charge transfer at active sites located in pores where electrolyte transport is facilitated whereas the second (Region 2) corresponds to reaction at less-accessible active sites in higher tortuosity flow channels. Likewise, two regions were also noted in the oxidation/reduction current profile for the pellets: an initial one (Region 1), where high current density values are attained due to mediation process at the active sites of the pellets that are easily accessible to the flow (large inter-pellet channels), and a second region, with significantly lower current density due to mediation at less-accessible sites (small intra-pellet channels), a slower process limited by diffusion of the electrolyte inside the pellets. While the "two-region behaviour" is similar for both monolith and pellets, the current density values of these regions are significantly different. This is attributed to contribution of the less-accessible active sites. While the contribution of these sites is significant for monolith due to the forced flow, this contribution is minor for pellets due to diffusion limitations. In Region 1 of monolith, less-accessible (small pores) and more-accessible (large pores) contribute. It is reasonable to assume that the more-accessible sites are converted faster, so that the Region 2 is governed by the contribution from less-accessible sites. However, the contribution of the less-accessible sites for pellets is much lower due to the lack of forced flow (diffusion limited). Thus, more-accessible (inter-pellets) sites are basically the only contributors for Region 1 and its value is lower than that obtained for monolith. Once the more-accessible sites are converted for pellets, the current for Region 2 becomes very small as only the less-accessible sites contribute to this region. Thus, reducing the difference in two different pore size populations through further optimization in the preparation of monolith is anticipated to result in further performance improvement. It should be noted that the redox mediator – solid booster pair of ferrocyanide/PB has an almost perfect match of their redox potentials. Thus, the importance of the solid booster confinement will be more critical for pairs in which the matching of their redox potentials is not perfect.

After demonstrating more efficient utilization of the solid booster with the monolith configuration, the cycling stability of this novel "flow-through" solid booster package was investigated. Specifically, symmetric ferro/ferricyanide redox mediated flow cells with PB booster monolith was subject to oxidation/reduction cycles using a potentiostatic protocol (±0.35 V and current density cut-off of ± 10 mA cm^{-2}) to achieve high depth of charge/discharge in short times. The symmetric flow cells consisted of 50 mL of a 0.2 M $K_4Fe(CN)_6$ and 0.1 M $K_3Fe(CN)_6$ mixture in the NCLS and 14 mL of 0.2 M $K_3Fe(CN)_6$ plus a booster monolith (medium sized, 1.235 g, 0.987 g of PB), or the equivalent amount of pellets (1.296 g, 1.040 g of PB), in an external tank in the CLS. Additionally, the cycling stability of a symmetric flow cell containing another monolith (medium sized, 1.280 g, 1.020 g of PB) was evaluated inside an Ar-filled glovebox. Note that content of 1 g of PB was used to minimize the error in the estimation of utilization rate, as discussed below in Section 2.5. The experiments were designed to i) compare the cycling stability of pellets and monoliths (Figure S16, Supporting Information), and ii) the influence of the presence of oxygen in cycling stability by operating outside and inside an Ar-filled glovebox (**Figure** 4). It should be noted that oscillations are due to temperature fluctuation between night and day. The values obtained during the day (22 °C) over several days are used to estimate the capacity fading. Figure S16 (Supporting Information) shows that a similar value was obtained for pellets and monolith outside the glovebox (capacity fading of 0.24 and 0.19% day^{-1} for pellets and monolith, respectively). This comparison shows that the confinement method does not affect significantly the capacity fading, which indicates that chemical degradation is the main source. More interestingly, the capacity fading did change significantly depending on whether the presence of oxygen was excluded or not. Figure 4 shows that while the charge capacity for the experiment carried out outside the Ar-filled glovebox decays gradually (capacity decay of 0.19% day^{-1}), the capacity of the setup evaluated inside the glovebox did not undergo any fading. In fact, the

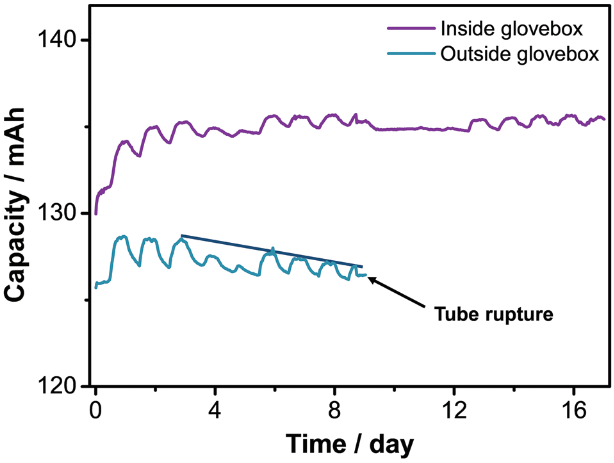

Figure 4. Evolution of capacity with time during oxidation/reduction cycling (potentiostatic protocol ±0.35 V and ±10 mA cm^{-2} current density cut-off) of a symmetric flow cell with 50 mL with 50 mL of a 0.2 M $K_4Fe(CN)_6$ and 0.1 M $K_3Fe(CN)_6$ mixture in the NCLS and 14 mL of 0.2 M $K_3Fe(CN)_6$ plus a medium size monolith operated inside and outside an Ar-filled glovebox. Oscillations are due to variation in temperature during night and day. Duration of oxidation steps (and reduction steps) were ca. 20 min.

capacity slightly increased during the first 2–3 days, stabilizing for the last 14 days. It should be noted that capacity increased during the first 1-1.5 days in systems with different monoliths tested (Section S7; Figure S17, Supporting Information). This behaviour is attributed to full soaking of the monoliths taking more than a day. Thus, the cell inside the Ar-filled glovebox delivered a capacity ≈ 135 mAh, which is 60 mAh above the theoretical value of the electrolyte, leading to 59 mAh g^{-1} (73.5% utilization rate) for the last 14 days. Two main conclusions are drawn from these experiments. I) The confinement method does not affect significantly the capacity fading, which indicates that chemical degradation is the main source. II) The presence of oxygen in the electrolyte has a major role in the capacity fading. In particular, no capacity fading was observed inside the glovebox during 17 days, so it can be concluded that the species generated from the reduction of oxygen are likely responsible for the capacity fading.

The high capacity retention value for the monolith inside the glovebox (no capacity decay for 17 days) suggests that the monolith does not undergo structural damage. Nevertheless, mercury porosimetry measurements were conducted before and after electrochemical cycling for 7 days. The comparison of the pore size distributions before and after electrochemical cycling for 7 days (Figure S15, Supporting Information) does not reveal any significant changes, which indicates that the electrolyte flow-through the monolith apparently does not impact its structural integrity as the monolith does not undergo structural damage.

Benchmarking of performances for redox-mediated flow batteries must be conducted with caution due to the lack of standardization in the testing conditions and its influence on the performance. For instance, in this work the utilization rate using monolith booster confinement varies from 67% to 83%, and the capacity decay from 0.19% day^{-1} for 9 days to no decay for 17 days, depending on the operation conditions. This shows the need for standardization in this emerging field to be able to conduct inter-laboratory comparisons. Nevertheless, Table S4 (Supporting Information) summarizes the performance reported in literature. While the utilization rate and cycling stability achieved in this work generally outperform the values reported in literature, it should be stressed that solid booster confinement in the form of monolith mainly benefits kinetics, which is of key importance in practical uses.

2.4. Pressure Drop Induced by the Flow-Through Booster Architecture

A critical aspect for RMFB systems that deploy the flow-through booster architecture is the pressure drop induced by the monolith, and the consequent increase in pump work and lower energy efficiency. However, direct estimation of the pump consumption induced by the monolith in standard lab-scale redox flow battery setups is not straightforward. The consumption of a standard peristaltic pump (MasterFlex L/S) for a standard lab bench redox flow battery setup is ≈ 11 W. The power delivered by these setups (single cell and 10 cm^2) varies between 0.2 and 1 W, depending on the cell voltage and current density of the system. Thus, the consumption of the pump is at least one order of magnitude higher than the power delivered by the system. Additionally, since these standard pumps are oversized, their consumption does not vary when the electrochemical cell, monolith or pellets are included in the systems). Consequently, we evaluated the pressure drop as an indirect measure of the impact of the monolith in the pump consumption (and energy efficiency) since energy consumption is proportional to the pressure drop induced by the monolith. To benchmark its contributions, the pressure drop induced by the electrochemical cell was also estimated as reference value. Numerical simulations were carried out to determine the theoretical pressure drop, as experimental values may be interfered by other factors, for example differences in porosity, tortuosity when the monolith size is changed. First, we studied the influence of the monolith (reservoir) geometry in the pressure drop. Two scenarios were evaluated; variation of the monolith height while keeping its diameter constant (**Figure 5A**; Figure S4, Supporting Information) and variation of the monolith diameter while keeping its height constant (Figure 5B; Figure S5, Supporting Information). It should be noted that dimensionless height and diameter are used for X-axis to simplify the comparison. The dimensionless values result from normalizing the height and diameter by the height (H_0 = 0.684 cm) and diameter (D_0 = 2.082 cm) of our standard size monolith (Figure S3, Supporting Information). The pressure drop induced by the monolith increased nearly linearly with the height while maintaining diameter. Nevertheless, the pressure drop induced by the monolith was more sensitive to changes in diameter. The decrease in pressure drop with increasing diameter was almost exponential. A third scenario was included. In this case, the volume of the monolith (reservoir) was maintained constant, which better illustrates how the pressure drop for a monolith of a given size can be tuned by changing its geometry. To maintain the volume constant at 2.33 cm^3 (volume of our standard size monolith having H_0 and D_0), the diameter of the monolith (upper X-axis) decreases as the height (bottom X-axis) increases. Figure 5C shows that pressure drop is minimized by increasing the diameter and reducing the height. A pressure

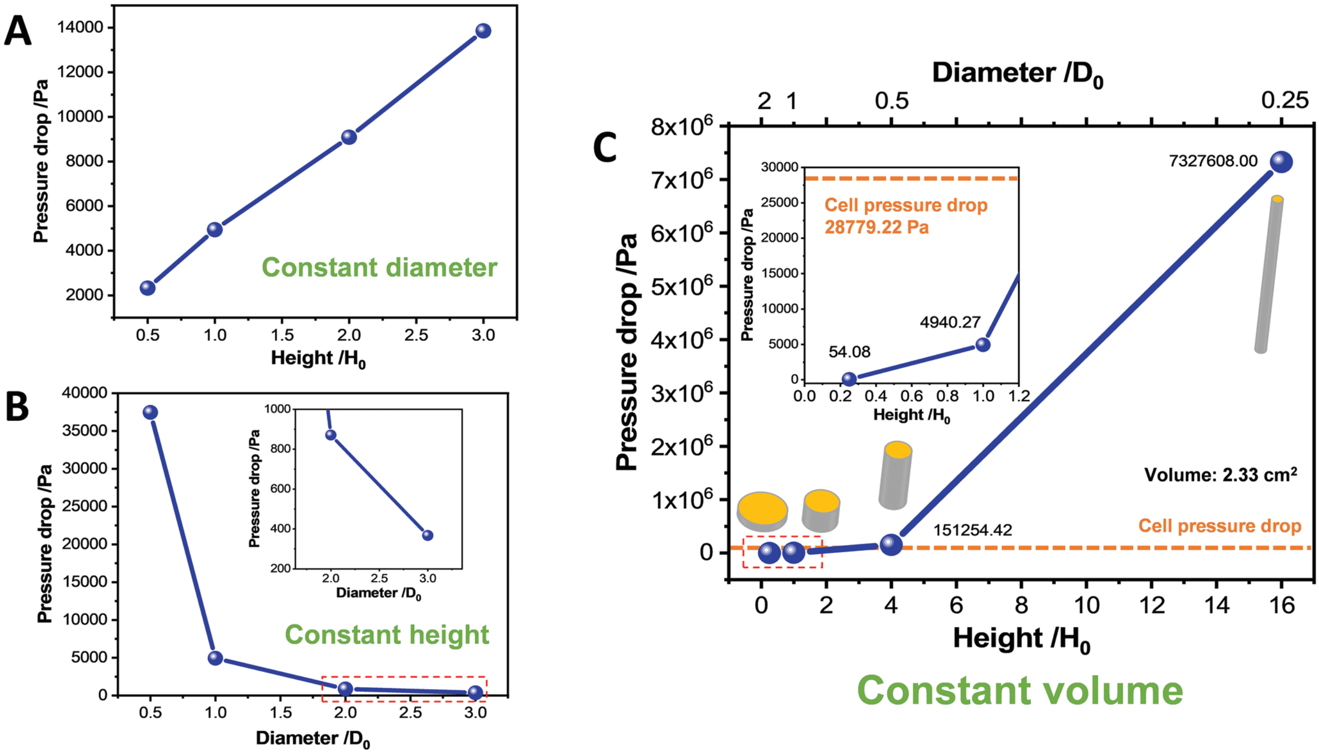

Figure 5. Geometry effects on the pressure drop of the monolith, where the values are normalized by our standard size monolith with a diameter of 2.082 cm (D_0) and a height of 0.684 cm (H_0) is used for comparison. A) Pressure drop of the monolith with different heights while keeping the diameter constant. B) Pressure drop of the monolith with different diameters while keeping the height constant. C) Pressure drop of the monolith with different diameters and heights while keeping the volume constant. The inserted figures are enlarged parts highlighted with red boxes.

drop of 54 Pa was achieved for a diameter of 4.164 cm (2 D_0, that is twice the standard diameter) and height of 0.171 cm (0.25 H_0, that is a quarter of standard height). To contextualize the relevance of this value, the pressure drop induced by the electrochemical cell was estimated. A conventional compressed carbon felt of 10 cm x 10 cm x 0.2 cm (detailed in Section S1, Supporting Information) exhibits a pressure drop of 28 779 Pa. In contrast, our standard geometry for 1 g of PB already shows a significantly lower pressure drop (4940 Pa), and the optimized design (54 Pa) effectively minimizes pump work (0.2% of the cell value), making it suitable for practical applications. This value can further be reduced since the electrochemical cell is oversized (10 cm^2 can deliver 500 mA) for 1 g of PB (60 mAh). Thus, a larger volume of the monolith (ninefold for 1 h storage) will enable further decrease in height and increase in diameter leading to even lower pressure drop.

Porosity and tortuosity of the monolith are two key parameters for the pressure drop as well as the electrochemical performance. However, decoupling of the influence of these two parameters is complex both from a theoretical and experimental perspective. In ANSYS FLUENT, these two parameters can be set independently. If porosity is adjusted without correspondingly modifying the permeability resistance coefficient and inertial resistance coefficient, there will be no significant changes in the pressure field in the simulation results. Therefore, in this calculation, the primary role of porosity is to determine the effective volume available for the fluid. It does not affect the pressure drop (Figure S9, Supporting Information), unless it is coupled with permeability and resistance coefficients. The pressure drop is generally governed by the resistance characteristics of the porous medium rather than by porosity. From an experimental viewpoint, 19 additional monoliths were prepared by changing several parameters in order to obtain monoliths with different porosities (Table S5, Supporting Information). Unfortunately, it was not possible to reduce significantly the porosity since the lowest value achieved was 63%. It seems that the density and particle size of the booster dominate the porosity of the monolith. Further reduction of porosity will likely require changes in the solid booster composition, which will induce other changes, for example kinetics. In addition, tortuosity cannot be maintained constant when porosity is changed. In fact, the role of this parameter is as important as porosity, like anticipated by the theory. For example, the two monoliths having 63.93% and 65.99% porosity behave very differently. The electrochemical performance of the monolith with 63.93% porosity (Figure S18, Supporting Information) is similar to the other monoliths discussed so far, indicating a homogenous distribution of the flow inside the monolith, while the other monolith with 65.99% porosity did not even allow the flow to go through at the standard pumping conditions. To unambiguously investigate these two key parameters, the fabrication of monolith must be changed. For instance, 3D printing or the use of 3D templates (coating of 3D structure) may enable relevant studies in this direction. While these types of fabrication may not be the best choice from a practical view, they will enable gaining fundamental understanding on key parameters.

2.5. Validation of the Equation to Predict Theoretical Charge Capacity

Finally, the advantageous features of a monolithic booster allowed us to investigate the validity of the fundamental equation widely used to predict the theoretically achievable charge storage capacity of a RMFB based on the volumetric capacities of solid (C_{solid}) and electrolyte ($C_{electrolyte}$), porosity of the solid material (β), utilization rate (α) and volumetric fraction of active material in the solid (γ):

$$C_{T,reservoir} = \alpha(1-\beta)\,\gamma\,C_{solid} + \beta\,C_{electrolyte} \tag{1}$$

In contrast to conventional redox flow batteries for which energy density is directly estimated from the charge experimentally stored and the volume of electrolyte added, RMFB contains two electroactive species, dissolved redox species and solid booster, having significantly different volumetric capacities. At lab scale, the ratio between the amount of the two types of electroactive species is far from that in large-scale systems. The relatively large amount of electrolyte outside the reservoir, compared to the amount inside the reservoir, makes the experimental estimation of energy density less straightforward. As a result, few experimental parameters are measured, and the practical energy density is calculated. However, to the best of our knowledge, this critical equation has not been validated. Fortunately, monoliths occupying the entire volume of the reservoir are prepared before assembly of the system. Thus, actual α and β are measured since the porosity of the tank corresponds to the porosity of the monolithic booster. In addition, the volume of the reservoir is known as the monolith occupies the entire space, allowing us to estimate its volumetric capacity as conventional RFBs. When conventional small-size pellets or granules are used, the inter-pellet porosity is complicated to be determined and the volume of the reservoir does not match the sum of the volumes of pellets. In other words, determination of the electrolyte volume between pellets is difficult, and it is not considered in the equation.

To compare practical capacity values measured with those predicted by theory, a large number of tests were conducted, comprising monoliths with 4 different sizes (ranging from 0.8 to 14 mL) and 3 compositions (from 75–85% active material) tested under different operating conditions, namely current density (10–30 mA cm^{-2}), electrolyte concentration (0.1–0.3 M) and electrolyte volume (10–14 mL). Table S6 (Supporting Information) summarizes the main characteristics of the monoliths prepared (size, composition, weight, volume, and porosity). Monolith size was coded according to the size of the mould used for the preparation as S for small, M for medium, L for large, and XL for extra-large. It should be noted that the apparent utilization rate of 0.33 for the only small monolith is attributed to an estimation error due to the low content of PB (0.3 g). The charge storage in the solid booster is determined from the difference between the measured capacity and the theoretical capacity of the electrolyte. In practice, theoretical capacity is not reached, introducing an error in the estimation. This error becomes negligible as the solid booster amount increases. Consequently, we recommend the use of at least 1 g of solid booster to prevent this error from occurring. Volume of each monolith was determined both from the volume of each component in the solid (estimated $V_{E,\,monolith}$) and from its dimensions measured with a caliper (measured $V_{M,monolith}$) (details in Section S10, Supporting Information). In the first case, $V_{E,\,monolith}$ was estimated from the porosity of solid material (β) and total volume of solid (V_{solid}) which is the sum of volumes of each component determined from their weight in the solid and the density (Equations S7 and S8, Supporting Information). In the case of measured $V_{M,\,monolith}$, it corresponded to the geometrical volume of a cylinder of height and diameter measured by a caliper. As can be seen (Table S6; Figure S19, Supporting Information), both volume values converge for monolith sizes ≥ 4 mL whereas deviations (4-18%) were noted for smaller monoliths, indicating more experimental error in the measurement of smaller monolith dimensions (e.g., 1.51 cm diameter of the smallest vs 4.52 cm of the largest). It is worth noting the similar porosity values of all monoliths prepared were obtained (71 ± 1%) regardless of their size and composition.

Theoretical and practical storage capacities for the CLS both excluding and including the volume of the tubes, together with utilization rates of the solid active material, are summarized in Table S7 (Supporting Information) for the different monoliths and test conditions. Equations used to calculate each parameter are given in Section S10 (Supporting Information). Overall, high utilization rates of Prussian Blue were obtained in most cases (66 – 83%, using the theoretical value of 80 mAh g^{-1}) except for the smallest monolith (33%), which may be attributed to a combination of factors, e.g. higher error (small mass), higher pressure drop induced the formation of preferential paths (small section), shorter mediating times. As can be seen, utilization rate increased with increasing size of the monolith, increasing relative content of active material in the booster and decreasing current densities. As the theoretical volumetric storage capacity of the reservoir ($C_{T,\,reservoir}$) that is estimated by the proposed Equation (1) scales with the utilization rates, $C_{T,\,reservoir}$ also increase with increasing monolith size, increasing content of active material and at low current densities due to the higher utilization rates achieved in those cases.

With the aim of assessing the validity of Equation (1) to predict $C_{T,\,reservoir}$, the practical volumetric capacity of the reservoir ($C_{P,\,reservoir}$) was determined by subtracting from the total practical capacity measured ($C_{P,\,CLS}$) the contribution of electrolyte in tubes and electrochemical reactor, and assuming that the volume of the reservoir is that of the monolith ($V_{M,monolith}$), as indicated in Section S10 (Equations S16–S18) (Supporting Information). As overall trend, practical capacity values ($C_{P,\,reservoir}$) approach theoretical ones ($C_{T,\,reservoir}$) as monolith size increases (Table S7, Supporting Information), becoming identical for the largest monolith (volume ≈ 14 mL). This trend is clearly observed in **Figure 6**, where the ratio between practical and theoretical volumetric capacities of the reservoir is plotted versus monolith volume for all tests. Deviations between predicted and actual capacity values are almost minimal (≈6%) for monolith volumes ≥4 mL but become more pronounced (≤15%) in smaller monoliths (< 4 mL). Indeed, these deviations mirror the trend for deviation between estimated and measured monolith volume values (Figure S19, Supporting Information), which also decreases as monolith size increases. Since $C_{P,\,reservoir}$ is calculated using measured monolith volumes ($V_{M,\,monolith}$), the larger deviations between practical and predicted capacities for small monoliths can be attributed to a lower accuracy of

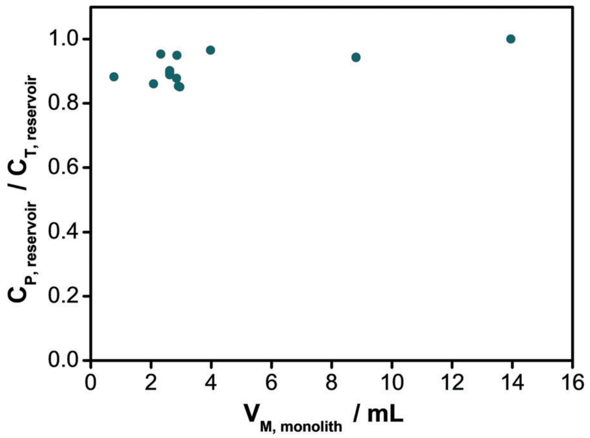

Figure 6. Ratio between practical capacity ($C_{P,\ reservoir}$) and theoretical volumetric capacity of the reservoir ($C_{T,\ reservoir}$) versus monolith size for all the monoliths tested.

monolith dimension measurements. Thus, our experimental results with monolithic boosters show that it is possible to reach volumetric capacity values theoretically predicted by the standard equation (but so far not validated) when scaling up tank size. If the full volume of the flow cell compartment (including reservoir, tubes, and electrochemical reactor) is taken into account to calculate the total practical volumetric capacity ($C_{P,\ CLS}$, Equation S19, Supporting Information), larger deviations from the theoretical $C_{T,\ reservoir}$ (only considering reservoir) are encountered in all tests (Table S7; Figure S20, Supporting Information). Nevertheless, total practical volumetric capacity and the theoretical volumetric capacity tend to converge as monolith size increases. That is, our results not only validate the equation at the tank level, but also prove that total practical and theoretical volumetric capacity values also converge at large tank volumes, as contribution of electrolyte in tubes (which is overlooked by the standard equation) becomes comparatively smaller. As a summary, packing solid booster materials in a monolithic configuration allowed us to validate the equation commonly used in literature to estimate the maximal theoretical capacity of RMFB. Our experimental results with several monolith sizes corroborate the validity of this established assumption for large-scale RMFB prototypes.

3. Conclusion

The proof of concept of a novel strategy for efficient packing of solid capacity boosters for redox mediated flow batteries in monolithic structures, combined with 3-D fabrication of a customized external reservoir, was demonstrated in this work. The proposed confinement concept was showcased with Prussian blue monoliths placed in the capacity limiting side of a symmetric potassium ferro/ferricyanide flow cell. The monolith manufacturing methodology developed is straightforward, easily scalable and versatile, allowing to vary key parameters that determine the energy storage performance of the solid booster, namely composition, dimensions and material packing/porosity. Confinement of the solid booster material in a single monolith densely packed in a fixed position in the external tank proved advantageous over conventional booster package formats (particles, granules or pellets), which are not immobilized in the tank. As predicted by fluid dynamic simulations, a filtering effect of the electrolyte "flowing-through" the whole booster material was ensured with the monolith configuration, minimizing dead volume and preventing formation of preferential flow pathways that occur in tanks with mobile booster particles, where electrolyte "flows-by". The facilitated fluid dynamics, with efficient diffusion of redox mediator to the electroactive sites in the monolith, resulted in high utilization rates of Prussian blue (66-83%) in a large number of monoliths prepared with different compositions and sizes. Indeed, comparative power tests with a same loading of booster material in the tank in the form of monolith and pellets revealed more efficient utilization of the solid booster with the monolith configuration, which delivered (twice) higher capacity in (20%) shorter times. Remarkably, the electrolyte flow-through the monolith did not impact its structural integrity, as the charge storing capacity of the monolith package remained stable showing no decay in 17 days upon cycling. Moreover, it was shown that the booster material was densely packed in the monolith, without inducing significant pressure drops that would impact pump energy consumption. Indeed, numerical simulation demonstrated how pressure drop can be minimized by tuning monolith geometry (height and diameter ratio) to become negligible compared to the pressure induced by the electrochemical cell, of relevance for engineering of scaled up booster tanks. In addition to practical and engineering benefits, the unique monolith configuration also showed advantages from a more fundamental point of view. Thus, the monolith booster allowed us to validate for the first time the theoretical equation used in literature to extrapolate the achievable energy density of new RMFB chemistries. This was now possible since the actual porosity of the reservoir, which is that of the monolith occupying the full reservoir volume, can be accurately determined. Very similar porosities were noted (71 ± 1%) in a large number of monoliths prepared (≈30), highlighting the reproducibility of the manufacturing method. Comparison of practical and theoretical charge storage capacity values for flow cells with a large number of different sized monoliths operated under several experimental conditions (electrolyte volume and concentration, current density) concluded that both values converged as monolith size increased. The deviations between practical and predicted capacities for small monoliths were attributed to a lower accuracy of monolith dimension measurements. Thus, our experimental results with monolithic boosters showed that it is possible to reach volumetric capacity values theoretically predicted by the standard equation (but so far not validated) when scaling up tank size.

In summary, the benefits of booster confinement as a monolith in the external tank of a RMFB have been demonstrated with a well-established redox mediator/solid booster system in a symmetric flow cell. We believe that the concept can be extended to other RMFB chemistries since the straightforward, reproducible, scalable and versatile monolith manufacturing methodology can be easily implemented in other solid booster materials.

4. Experimental Section

Materials: All reagents and solvents were analytical grade and used as received without further purification. Potassium ferrocyanide trihydrate, potassium ferricyanide, iron (III) hexacyanoferrate (II), polyvinylidene fluoride and N-methyl-2-pyrrolidone were purchased from Thermoscientific. Potassium chloride was purchased from Aldrich and Ketjen Black from Nanografi. Standard clear resin of the 3D printer was purchased from Anycubic. Solutions were prepared using deionized water.

Preparation of PB Pellets: PB pellets were prepared by extruding a mixture of PB, KB and PVDF in NMP with a 80:10:10 (LFP:KB:PVDF) composition from a 20 mL-syringe. Obtained filaments with 2 mm diameter were cut into 7 mm length pieces and dried in an oven at 100 °C for 24 h.

Flow Cells: Filter-pressed flow cell using Nafion 212 and graphite felt as the ion selective membrane and electrodes were used for the flow experiments. Graphite felt was activated with potassium hydroxide. In some experiments, copper endplates were placed in both sides of the filter-pressed flow cell. The projected area of the cell was 10 cm^2 and the flow rate was fixed at 30 mL min^{-1} (MasterFlex L/S peristaltic pump motor and Easy-Load 3 Pump Heads). General conditions for the flow cell were: non-capacity limiting side (NCLS): 50 mL of a mixture of $K_4Fe(CN)_6$ and $K_3Fe(CN)_6$ in 1.0 м KCl (varying concentrations between 0.1-0.2 M); capacity limiting side (CLS): 10–14 mL of 0.1 M-0.3 м of $K_4Fe(CN)_6$ or $K_3Fe(CN)_6$ in 1.0 м KCl, adding the booster (monolith or pellets) to this side.

Electrochemical Characterization: Electrochemical measurements were performed using two battery testing systems (BTS), Neware BTS models CT-4008T-5V6A-S1 and CT-4008Tn-5V6A-S1-F. Potassium ferro/ferricyanide symmetric cells were galvanostatically oxidised/reduced at different current densities of ±10–30 mA cm^{-2} with voltage limits of ±0.35 V. Cycling tests of potassium ferro/ferricyanide symmetric cells were also conducted by the constant current followed by constant voltage (CCCV) protocol, applying a constant current density of ±20 mA cm^{-2} with cut-off values of ±0.3 V, followed by a constant charging/discharging voltage of ±0.3 V until the current dropped to ±10 mA cm^{-2}.

Pressure Drop Measurements: Evaluation of pressure changes induced by the booster package was done with a compact pressure transmitter, Danfoss MBS 1700, suited to measure in the relative pressure range 0–10 bar (Figure S6, Supporting Information). The output signal of the transmitter is a 4–20 mA current, which is proportional to the input pressure value (Section S1, Supporting Information).

Mercury Porosimetry: Porosity was measured using a Micromeritics AutoPore IV 9500 porosimeter, manufactured by Micromeritics Instrument Corporation. The porosimeter utilized a range from 100 µm down to 1 nm (pore size diameter), applying pressures ranging from 0 to 200 MPa in step mode. A contact angle of 135 °was assumed for the calculations.

Numerical Modeling: A 3D numerical calculation based on the finite volume method (FVM) was performed by ANSYS Fluent 2022, where pressure-velocity coupling is in coupled scheme and Rhie-Chow. A Navier-Stokes equation incorporated with porous media model was calculated as detailed in Section S1 (Supporting Information).

Supporting Information

Supporting Information is available from the Wiley Online Library or from the author.

Acknowledgements

The authors acknowledge financial support by the Spanish Government Agencia Estatal de Investigación/Ministerio de Ciencia e Innovación, Grants PID2021-124974OB-C22, PID2023-148198NB-C21, CNS2023-145051, and Ramon y Cajal award (RYC2018-026086-I), the MeBattery project (MeBattery has received funding from the European Innovation Council of the European Union under Grant Agreement no. 101046742) and the Regional Government of Castilla y Leon (NextGeneration EU/PRTR (C17. I1)). E.V. thanks the MINECO for the financial support (RYC2018-026086-I). G.M.T. acknowledges the fellowship from the Regional Government of Castilla y Leon (Junta de Castilla y León), which is partially supported by the European Social Fund.

Conflict of Interest

The authors declare no conflict of interest.

Data Availability Statement

The data that support the findings of this study are available from the corresponding author upon reasonable request.

Keywords

flow-through, monoliths, redox flow batteries, redox mediators, solid boosters

Received: September 30, 2024
Revised: December 17, 2024

[1] P. Alotto, M. Guarnieri, F. Moro, *Renew. Sustain. Energy Rev.* **2014**, *29*, 325.
[2] E. Sánchez-Díez, E. Ventosa, M. Guarnieri, A. Trovò, C. Flox, R. Marcilla, F. Soavi, P. Mazur, E. Aranzabe, R. Ferret, *J. Power Sources* **2021**, *481*, 228804.
[3] E. Ventosa, *Curr. Opin. Chem. Eng.* **2022**, *37*, 100834.
[4] B. R. Chalamala, T. Soundappan, G. R. Fisher, M. R. Anstey, V. V. Viswanathan, M. L. Perry, *Proc. IEEE* **2014**, *102*, 976.
[5] a) R. Yan, Q. Wang, *Adv. Mater.* **2018**, *30*, 1802406; b) F. Zhang, M. Gao, S. Huang, H. Zhang, X. Wang, L. Liu, M. Han, Q. Wang, *Adv. Mater.* **2022**, *34*, 2104562.
[6] a) Z. Qi, G. M. Koenig, *J. Vac. Sci. Technol. B* **2017**, *35*, 040801; b) S. Gentil, D. Reynard, H. H. Girault, *Curr. Opin. Electrochem.* **2020**, *21*, 7.
[7] D. Gupta, Y. Zhang, Z. Nie, J. Wang, G. M. Koenig Jr, *Chem. Eng. Sci.* **2022**, *251*, 117443.
[8] a) F. Pan, J. Yang, Q. Huang, X. Wang, H. Huang, Q. Wang, *Adv. Energy Mater.* **2014**, *4*, 1400567; b) J. Li, L. Yang, B. Yuan, G. Li, J. Y. Lee, *Mater. Today Energy* **2017**, *5*, 15; c) C. M. Wong, C. S. Sevov, *ACS Energy Lett.* **2021**, *6*, 1271.
[9] E. Schröter, C. Stolze, A. Saal, K. Schreyer, M. D. Hager, U. S. Schubert, *ACS Appl. Mater. Interfaces* **2022**, *14*, 6638.
[10] a) T. Páez, A. Martínez-Cuezva, J. Palma, E. Ventosa, *ACS Appl. Energy Mater.* **2019**, *2*, 8328; b) T. Páez, F. Zhang, M. Á. Muñoz, L. Lubian, S. Xi, R. Sanz, Q. Wang, J. Palma, E. Ventosa, *Adv. Energy Mater.* **2022**, *12*, 2102866; c) S. Berling, J. M. Hidalgo, N. Patil, E. García-Quismondo, J. Palma, C. Ponce de León, *J. Energy Storage* **2023**, *68*, 107620.
[11] a) J. F. Vivo-Vilches, A. Nadeina, N. Rahbani, V. Seznec, D. Larcher, E. Baudrin, *J. Power Sources* **2021**, *488*, 229387; b) J. F. Vivo-Vilches, Á. Vázquez-Navalmoral, C. de la Torre-Gamarra, J. Cebollada, A. Várez, B. Levenfeld, *Batter. Supercaps* **2022**, *5*, 202200050.
[12] a) Y. Cheng, X. Wang, S. Huang, W. Samarakoon, S. Xi, Y. Ji, H. Zhang, F. Zhang, Y. Du, Z. Feng, S. Adams, Q. Wang, *ACS Energy Lett.* **2019**, *4*, 3028; b) M. Zhou, Q. Huang, T. N. Pham Truong, J. Ghilane, Y. G. Zhu, C. Jia, R. Yan, L. Fan, H. Randriamahazaka, Q. Wang, *Chem* **2017**, *3*, 1036; c) J. Yu, L. Fan, R. Yan, M. Zhou, Q. Wang, *ACS Energy Lett.* **2018**, *3*, 2314; d) S. Huang, H. Zhang, M. Salla, J. Zhuang, Y. Zhi, X. Wang, Q. Wang, *Nat. Commun.* **2022**, *13*, 4746; e) Y. Chen, M. Zhou, Y. Xia, X. Wang, Y. Liu, Y. Yao, H. Zhang, Y. Li, S. Lu, W. Qin, X. Wu, Q. Wang, *Joule* **2019**, *3*, 2255.